The First Result of Land Surface Temperature Retrieval From SDGSAT-1 Thermal Imager Spectrometer

Weihan Liu and Jie Cheng, *Senior Member, IEEE*

***Abstract*— This letter reported the first land surface temperature (LST) retrieval result from the thermal infrared spectrometer (TIS) onboard the Sustainable Development Science Satellite 1 (SDGSAT-1). The LST was retrieved from the three TIS thermal infrared (TIR) channels by a temperature and emissivity separation (TES) algorithm, which was adapted from an improved TES (iTES) algorithm. In situ validation showed the TIS iTES algorithm achieved a bias of 0.16 K and an RMSE of 3.01 K at SURFRAD sites. The radiance-based validation indicated the bias and RMSE of the retrieved LST are −0.49 and 2.71 K, respectively. In addition, cross-comparison with MYD21 LST showed that the retrieved LST had an average bias and RMSE of 1.15 and 1.80 K, respectively. These results demonstrated that the developed iTES algorithm is capable of retrieving LST from SDGSAT-1/TIS data with acceptable accuracy. This study provides a practical method of deriving LST from SDGSAT-1/TIS data and facilitates the application of SDGSAT-1/TIS data in studies related to thermal environment monitoring, surface energy balance, and climate change.**

***Index Terms*— Land surface temperature (LST), Sustainable Development Science Satellite 1 (SDGSAT-1), temperature and emissivity separation (TES), thermal infrared spectrometer (TIS).**

I. INTRODUCTION

LAND surface temperature (LST) underpins the thermal exchange dynamics between land and atmosphere, earning its status as an essential climate variable (ECV) [1] due to its integral role in climate change research and Earth system science [2], [3]. Retrieval of LST from satellite thermal infrared (TIR) observations has seen significant achievements, highlighting its importance in environmental monitoring.

TIR LST retrieval algorithms can generally be categorized based on whether the land surface emissivity (LSE) is considered a priori [4]. For algorithms that use LSE as a priori information, this LSE is typically determined based on land cover classification or vegetation indices [5], [6]. However, an error of 0.01 in the preset LSE can cause an LST retrieval error of over 0.6 K for land surfaces at temperatures ∼300 K [7]. The temperature and emissivity separation (TES) algorithm is a well-established method for simultaneously retrieving LST and LSE [8]. In regions with sparse vegetation or bare soil, where accurately predicting LSE is challenging, the TES algorithm can achieve higher accuracy in LST retrieval [9].

The Sustainable Development Science Satellite 1 (SDGSAT-1) emerges as a pioneering satellite, meticulously crafted to support the United Nations 2030 Agenda for Sustainable Development [10]. The TIR spectrometer (TIS) on SDGSAT-1, capturing thermal images at a 30 m high spatial resolution and boasting a swath of 300 km across three TIR atmospheric windows (8–10.5 μm, 10.3–11.3 μm, 11.5–12.5 μm), ensures the optimal configuration for TES algorithm application and has shown reliable calibration and noise performance in prelaunch tests [11].

Recently, the ASTER TES algorithm [8] was adapted to SDGSAT-1/TIS to retrieve lunar surface temperature and emissivity [12]. Given the Moon's lack of atmosphere, the TES algorithm does not need to consider the interference of the atmosphere and achieves lunar surface temperature accuracy better than 1 K based on simulations [12]. However, Earth's complex surface and atmospheric environment are totally different from the Moon, which presents challenges for the TES algorithm. To our knowledge, there are no publicly available SDGSAT-1/TIS algorithms for retrieving terrestrial LST and LSE.

Therefore, this study aims to extend our previously developed iTES algorithm to retrieve LST from SDGSAT-1/TIS data. The letter is organized as follows. Section II outlines the theoretical framework of the TES algorithm for SDGSAT-1/TIS. Section III presents the evaluation and analysis of the LST retrieval. Finally, the conclusion is offered in Section IV.

II. ITES ALGORITHM

Per radiative transfer theory, the top of the atmosphere (TOA) radiance detected by a TIR sensor's specific channel i can be concisely represented as follows:

$$L_i(\theta) = \left(\varepsilon_i(\theta)B_i(T_S) + (1-\varepsilon_i)L_i^{\downarrow}\right)\tau_i(\theta) + L_i^{\uparrow}(\theta) \quad (1)$$

where θ is the viewing zenith angle; ε_i is the LSE; T_S is the LST; $B_i(T_S)$ represents the Planck function at T_S; $\tau_i(\theta)$ is the

---

Manuscript received 4 April 2024; revised 10 June 2024; accepted 16 June 2024. Date of publication 19 June 2024; date of current version 1 July 2024. This work was supported in part by the National Natural Science Foundation of China under Grant 42071308 and Grant 42192581 and in part by the Second Tibetan Plateau Scientific Expedition and Research Program (STEP) under Grant 2019QZKK0206. *(Corresponding author: Jie Cheng.)*

Weihan Liu is with the School of Environment, Institute of Remote Sensing Science and Engineering, Faculty of Geographical Science, Beijing Normal University, Beijing 100875, China (e-mail: liuweihan@mail.bnu.edu.cn).

Jie Cheng is with the Institute of Remote Sensing Science and Engineering, Faculty of Geographical Science, Beijing Normal University, Beijing 100875, China (e-mail: jie_cheng@bnu.edu.cn).

Digital Object Identifier 10.1109/LGRS.2024.3416526

transmittance of the total atmosphere; $L_i^{\downarrow}$ is the hemispherical integrated atmospheric downward radiance; and $L_i^{\uparrow}(\theta)$ is the atmospheric upward radiance.

Guided by (1), the iTES algorithm incorporates two fundamental steps: atmospheric correction and TES. Specifically, the three atmospheric parameters ($\tau_i(\theta)$, $L_i^{\downarrow}$ and $L_i^{\uparrow}(\theta)$) are determined in the atmospheric correction, and an additional constraint enabling the three-band equation system to be well-posed is introduced in TES, facilitating the simultaneous decoupling of LST and LSE.

A. Atmospheric Correction

The atmospheric parameters were simulated by feeding the Modern-Era Retrospective analysis for Research and Applications version 2 (MERRA-2) atmospheric temperature and humidity profiles [13] into the moderate-resolution atmospheric transmission code (MODTRAN v5.2.2) [14].

The MERRA2 atmospheric profiles, compared to the ideal radiosonde measurements during SDGSAT-1/TIS overpasses, expose errors that affect LST accuracy, notably under humid conditions [15], [16]. The water vapor scaling (WVS) method improves atmospheric correction accuracy by reshaping atmospheric water vapor profiles [17], [18], and has been integrated into the developed SDGSAT-1/TIS iTES algorithm.

The WVS method originates from the extended multichannel (EMC)/water-vapor-dependent (WVD) algorithm [19], which utilizes TOA brightness temperature (BT) and total precipitable water (TPW) to approximate the surface BT

$$L_{g,i}(\theta) = B_i\left(T_{g,i}\right) = \frac{L_i(\theta) - L_i^{\uparrow}(\theta,\gamma)}{\tau_i(\theta,\gamma)}$$

with $T_{g,i} = \alpha_{i,0} + \sum_{k=1}^{\mathrm{n}} \alpha_{i,k} T_k$

$$\alpha_{i,k} = p_{i,k} + q_{i,k} W + r_{i,k} W^2 \tag{2}$$

where $L_{g,i}(\theta)$ is the ground-leaving radiance; $T_{g,i}$ is the surface BT; $\tau_i(\theta,\gamma)$ and $L_i^{\uparrow}(\theta,\gamma)$ are the atmospheric transmissivity and the atmospheric upwelling radiance with the water-vapor profile scaled by factor γ; T_k is the TOA BT measured by channel k; α, p, q, and r are the EMC/WVD coefficients for each channel; and W denotes the TPW.

When utilizing the Pierluissi double exponential band model [20] to approximate the atmospheric transmittance, the $\tau(\theta,\gamma)$ and $L^{\uparrow}(\theta,\gamma)$ in (2) can be expressed as

$$\tau(\theta,\gamma) = \tau(\theta,\gamma_1)^{\gamma^a - \gamma_2^a / \gamma_1^a - \gamma_2^a} \cdot \tau(\theta,\gamma_2)^{\gamma_1^a - \gamma^a / \gamma_1^a - \gamma_2^a} \tag{3}$$

$$L^{\uparrow}(\theta,\gamma) = L^{\uparrow}(\theta,\gamma_1) \cdot \frac{1-\tau(\theta,\gamma)}{1-\tau(\theta,\gamma_1)} \tag{4}$$

where C is the band model absorption coefficient, U is the scaled absorber amount, a is the band model parameter, and γ_1 and γ_2 are two given different scaling factor values.

Based on the SDGSAT-1/TIS spectral response function, the EMC/WVD coefficients in (2) were fit using training data created from MODTRAN simulations, incorporating atmospheric profiles from the SeeBor V5.0 database [21] and emissivity spectra from ASTER and MODIS spectral libraries. With the modeled atmospheric transmittance under different WVS factors (γ, γ_1 and γ_2) in (3) set to 0.9, 0.7, and 1.0, respectively, the band model parameter a was then optimized utilizing a boundary-constrained modification of the Nelder-Mead simplex algorithm [22].

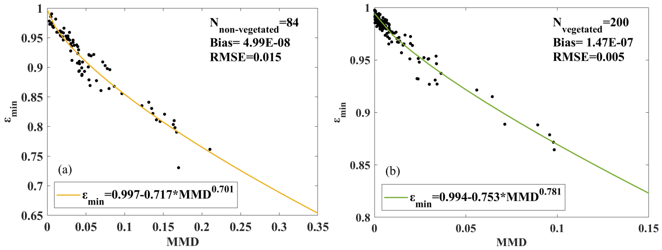

Fig. 1. Fit MMD empirical functions for SDGSAT-1/TIS. (a) General curve fit with 84 ASTER emissivity spectra and (b) new curve fit using 200 4SAIL-simulated emissivity spectra over vegetated surfaces.

Inserting (3) and (4) into (2) yields the formulation calculating the scaling factor γ for each pixel in real-time across three TIR bands during the retrieval process

$$\gamma = \left(\frac{\ln\left(\frac{\tau(\theta,\gamma_2)^{\gamma_1^a}}{\tau(\theta,\gamma_1)^{\gamma_2^a}} \cdot \frac{B\left(T_g\right) - \frac{L^{\uparrow}(\theta,\gamma_1)}{1-\tau(\theta,\gamma_1)}}{L(\theta) - \frac{L^{\uparrow}(\theta,\gamma_1)}{1-\tau(\theta,\gamma_1)}} \right)^{\left(\gamma_1^a - \gamma_2^a\right)}}{\ln\left(\frac{\tau(\theta,\gamma_2)}{\tau(\theta,\gamma_1)} \right)} \right)^{1/a}. \tag{5}$$

Note that the channel index i is omitted in (3)–(5) for simplicity.

B. Temperature and Emissivity Separation

TES integrates the normalized emissivity method (NEM) module, emissivity ratio module, and maximum-minimum difference (MMD) module [8]. Initially, all maximum channel emissivity were set to 0.99, iteratively refined through NEM, and then normalized by their average. An empirical function linking the minimum emissivity with the MMD of normalized emissivities was used to calculate the minimum emissivity, enabling LST computation.

To develop the empirical function of the TES-MMD module for SDGSAT-1/TIS, 84 emissivity spectra from the ASTER spectral library, encompassing rocks, soils, water, and ice/snow samples, were selected to fit the MMD empirical function for nonvegetated surfaces. To boost the TES accuracy within vegetated areas, the MMD module was further improved using a recalibrated empirical function fit using the canopy emissivity spectra simulated by scattering by arbitrary inclined leaves (4SAIL) model [23], mitigating LST overestimation by accounting for the cavity effect in soil-vegetation system [24]. Fig. 1 shows the fit MMD empirical functions for both nonvegetated and vegetated surfaces. During the retrieval process, when NDVI ≥ 0.2 [25], the pixel is labeled as vegetated, and the recalibrated function for vegetated surfaces is adopted.

TABLE I
INFORMATION OF SURFRAD IN SITU SITES FOR IN SITU VALIDATION

Identifier	Location	Climatic type*
BND	40.052°N, 88.373°W	Dfa
TBL	40.125°N, 105.237°W	BSk
DRA	36.624°N, 116.019°W	BWk
FPK	48.308°N, 105.102°W	BSk
GWN	34.255°N, 89.873°W	Cfa
SXF	43.734°N, 96.623°W	Dfa

* Koppen climate classification system [31]. Aw: tropical, savannah; BSh: arid, steppe, hot; BSk: arid, steppe, cold; BWk: arid, desert, cold; Cfa: temperate, no dry season, hot summer; Cfb: Temperate, no dry season, warm summer; Dfa: temperate, no dry season, hot summer.

TABLE II
INFORMATION OF UWYO RATIO SOUNDINGS FOR R-BASED VALIDATION

Identifier	Location	Climatic type*
YBCV/94510	26.410°S, 146.260°E	BSh
Woodstock/95282	19.630°S, 146.860°E	Aw
YPWR/94659	31.150°S, 136.810°E	BWh
Cobar Mo/94711	31.480°S, 145.830°E	BSh
YSWG/94910	35.160°S, 147.460°E	BSk
YPAD/94672	34.950°S, 138.520°E	BSk
YBBN/94578	27.390°S, 153.130°E	Cfa
YMML/94866	37.670°S, 144.830°E	Cfb

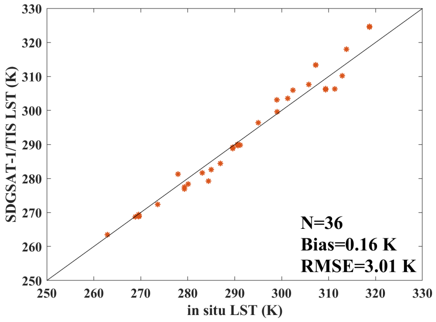

Fig. 2. In situ validation results of SGDSAT-1/TIS LST.

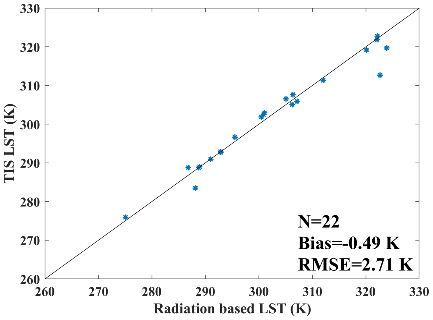

Fig. 3. SGDSAT-1/TIS LST R-based validation results.

III. RESULTS AND ANALYSIS

A. In Situ Validation

During the 15 months from October 2022 to December 2023, ground measurements from seven SURFace RADiation budget (SURFRAD) network sites [26] were collected for in situ validation. We obtained 82 spatial-temporal matched SDGSAT-1/TIS images in this period. In situ LST was calculated using the recorded upwelling and downward longwave radiation in combination with broadband emissivity (BBE) empirically converted from the ASTER narrowband emissivity data using the formula of [27]. During prolonged periods lacking ASTER overpasses, the Essential TIR remoTe sEnsing (ELITE) BBE [28], [29] was utilized as the supplement.

Table I details the SURFRAD sites. Fig. 2 presents the validation results of the retrieved SGDSAT-1/TIS LST. In total, we obtained 36 matchup, yielding a bias of 0.16 K and an RMSE of 3.01 K.

B. Radiation-Based Validation

The Radiation-based (R-based) LST validation method employs LSE and synchronized atmospheric profiles, functioning independently of ground-based LST measurements [31]. We sourced radiosounding data from 2023, at 0000 and 1200 Z throughout Australia, from the University of Wyoming (UWYO) upper air data archive, selecting only profiles with relative humidity under 90% at every level to avoid cloudy conditions. Due to its lower LSE uncertainty and minimal atmospheric absorption, TIS Band 3 was selected for R-based LST validation, with the LSE estimated from the ECOSTRESS band 5 LSE [32] by spectral conversion. Starting with the retrieved TIS LST as the initial input, MODTRAN simulations refine TOA radiation to match the satellite TOA measurements, iteratively optimizing the LST to achieve the R-based LST.

Table II catalogs the collected radiosounding information. Fig. 3 showcases the R-based LST validation results for SDGSAT-1/TIS. During the standard 00 and 12 Z sounding times and within a 30 min window, 37 SDGSAT-1/TIS images were collected. From these, 22 clear-sky LST retrievals were matched, revealing a bias of −0.49 K and an RMSE of 2.71 K.

C. Cross Validation

To assess the performance of the developed SDGSAT-1/TIS iTES algorithm, we compared the LST retrieved from two specific scenarios with the collocated MODIS MOD21 LST product [9]. Fig. 4(a) and (b) shows the comparison results in the Qinghai-Tibet Plateau, captured on June 23, 2023, at 1500 Z. Fig. 4(c) and (d) illustrates LSTs from TIS and MODIS in western North America's mountainous regions, observed on November 25, 2023, at 0500 and 0520 Z, respectively. Histograms in Fig. 4(e) and (f) details the LST differences across the two cases, showing the SDGSAT-1/TIS LST has a bias of 0.93 K and RMSE of 1.93 K in the first case, a bias of 1.38 K and RMSE of 1.67 K in the second, compared with the MOD21 LST. The cross-validation between SDGSAT-1/TIS LST and MOD21 LST reveals high similarity in overall patterns. Additionally, benefiting from higher spatial resolution, the SDGSAT-1/TIS LST presents enhanced detail in the LST color maps.

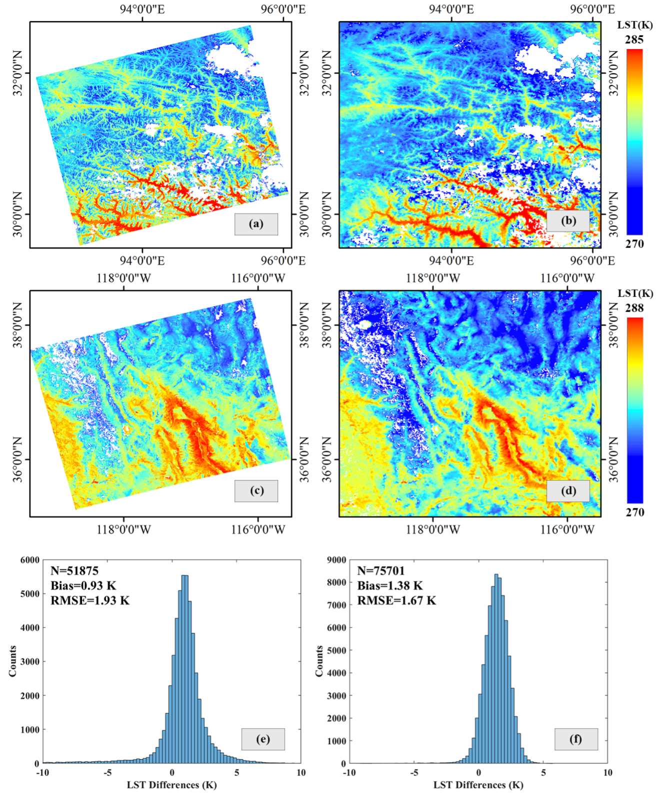

Fig. 4. Comparison of LSTs from SDGSAT-1/TIS and MOD21 in two cases: (a) and (b) SDGSAT-1/TIS LST, (c) and (d) MOD21 LST, and (e) and (f) histograms of the differences between SDGSAT-1/TIS LST and MOD21 LST.

IV. CONCLUSION

The LST plays an essential role in studying climate change and Earth system science. This letter extends the iTES algorithm to SDGSAT-1/TIS data to retrieve LST. The SDGSAT-1/TIS iTES algorithm involves two core contents: atmospheric correction and TES. Atmospheric parameters are simulated by inputting the MERRA-2 profiles into MODTRAN and refined by the WVS method. The MMD module was optimized for vegetated surfaces using a new empirical function constructed from the 4SAIL simulated canopy emissivity spectra.

In situ validation results at SURFRAD sites showed that the SDGSAT-1/TIS iTES algorithm achieved a bias of 0.16 K and an RMSE of 3.01 K of LST retrieval. Radiance-based validation indicated the bias and RMSE of the retrieved LST are -0.49 K and RMSE of 2.71 K, respectively. Finally, a comparison with MYD21 LST showed that the retrieved LST had an average bias and an RMSE of 1.15 K and 1.80 K, respectively. It should be noted that the first TIR band of SDGSAT-1/TIS covers part of the ozone absorption range around 9.6 μm, which may affect LST retrieval accuracy. Additionally, stripe noise is present in the on-orbit images captured by the SDGSAT-1/TIS [33]. Since data processing is not the focus of this study, stripe noise filtering was not performed before LST retrieval. Furthermore, the in situ LST calculations use a common simplified method that neglects near-surface atmospheric effects, potentially introducing errors in the in situ longwave radiations used for LST validation [34]. Nevertheless, the results showed that the developed iTES algorithm is capable of deriving LST from SDGSAT-1/TIS data with acceptable accuracy. In the next phase, we plan to collect additional TSI imagery and ground observation data for comprehensive validation and further improve the algorithm. This contribution is expected to enhance the application of SDGSAT-1/TIS data in studies related to thermal environment monitoring, surface energy balance, and climate change.

ACKNOWLEDGMENT

We gratefully thank the International Research Center of Big Data for Sustainable Development Goals for providing SDGSAT-1/TIS data.

REFERENCES

[1] A. Belward et al. (2016). *The Global Observing System for Climate: Implementation Needs*. [Online]. Available: https://library.wmo.int/doc_num.php?explnum_id=3417

[2] Z.-L. Li et al., "Satellite-derived land surface temperature: Current status and perspectives," *Remote Sens. Environ.*, vol. 131, pp. 14–37, Apr. 2013.

[3] J. Cheng, X. Meng, S. Dong, and S. Liang, "Generating the 30-m land surface temperature product over continental China and USA from Landsat 5/7/8 data," *Sci. Remote Sens.*, vol. 4, Dec. 2021, Art. no. 100032.

[4] J. Cheng, S. Liang, J. Wang, and X. Li, "A stepwise refining algorithm of temperature and emissivity separation for hyperspectral thermal infrared data," *IEEE Trans. Geosci. Remote Sens.*, vol. 48, no. 3, pp. 1588–1597, Mar. 2010.

[5] W. C. Snyder, Z. Wan, Y. Zhang, and Y.-Z. Feng, "Classification-based emissivity for land surface temperature measurement from space," *Int. J. Remote Sens.*, vol. 19, no. 14, pp. 2753–2774, Jan. 1998.

[6] E. Valor and V. Caselles, "Mapping land surface emissivity from NDVI: Application to European, African, and South American areas," *Remote Sens. Environ.*, vol. 57, no. 3, pp. 167–184, Sep. 1996.

[7] F. Becker, "The impact of spectral emissivity on the measurement of land surface temperature from a satellite," *Int. J. Remote Sens.*, vol. 8, no. 10, pp. 1509–1522, Oct. 1987.

[8] A. Gillespie, S. Rokugawa, T. Matsunaga, J. S. Cothern, S. Hook, and A. B. Kahle, "A temperature and emissivity separation algorithm for Advanced Spaceborne Thermal Emission and Reflection Radiometer (ASTER) images," *IEEE Trans. Geosci. Remote Sens.*, vol. 36, no. 4, pp. 1113–1126, Jul. 1998.

[9] G. Hulley, N. Malakar, and R. Freepartner, "Moderate resolution imaging spectroradiometer (MODIS) land surface temperature and emissivity product (MxD21) algorithm theoretical basis document collection-6.1," JPL Publication, pp. 12–17, Dec. 2016. [Online]. Available: https://lpdaac.usgs.gov/documents/1399/MOD21_ATBD.pdf

[10] H. Guo et al., "SDGSAT-1: The world's first scientific satellite for sustainable development goals," *Sci. Bull.*, vol. 68, no. 1, pp. 34–38, Jan. 2023.

[11] Z. Hu, M. Zhu, Q. Wang, X. Su, and F. Chen, "SDGSAT-1 TIS prelaunch radiometric calibration and performance," *Remote Sens.*, vol. 14, no. 18, p. 4543, Sep. 2022.

[12] Q. Wang, Z. Hu, L. Zou, and F. Chen, "Lunar surface temperature and emissivity retrieval from SDGSAT-1 thermal imager spectrometer," *IEEE Geosci. Remote Sens. Lett.*, vol. 20, pp. 1–5, 2023.

[13] R. Gelaro et al., "The modern-era retrospective analysis for research and applications, version 2 (MERRA-2)," *J. Climate*, vol. 30, pp. 5419–5454, Jul. 2017.

[14] A. Berk et al., "MODTRAN (TM) 5: A reformulated atmospheric band model with auxiliary species and practical multiple scattering options: Update," *Proc. SPIE*, vol. 5806, pp. 662–667, Jun. 2005.

[15] A. R. Gillespie, E. A. Abbott, L. Gilson, G. Hulley, J.-C. Jiménez-Mu noz, and J. A. Sobrino, "Residual errors in ASTER temperature and emissivity standard products AST08 and AST05," *Remote Sens. Environ.*, vol. 115, no. 12, pp. 3681–3694, Dec. 2011.

[16] G. C. Hulley, C. G. Hughes, and S. J. Hook, "Quantifying uncertainties in land surface temperature and emissivity retrievals from ASTER and MODIS thermal infrared data," *J. Geophys. Res., Atmos.*, vol. 117, no. D23, Dec. 2012.

[17] H. Tonooka, "Introduction of water vapor dependent coefficients to multichannel algorithms," *J. Remote Sens. Soc. Jpn.*, vol. 20, pp. 137–148, Jun. 2000, doi: 10.11440/rssj1981.20.137.

[18] H. Li et al., "Evaluation of atmospheric correction methods for the ASTER temperature and emissivity separation algorithm using ground observation networks in the HiWATER experiment," *IEEE Trans. Geosci. Remote Sens.*, vol. 57, no. 5, pp. 3001–3014, May 2019.

[19] C. Francois and C. Ottle, "Atmospheric corrections in the thermal infrared: Global and water vapor dependent split-window algorithms-applications to ATSR and AVHRR data," *IEEE Trans. Geosci. Remote Sens.*, vol. 34, no. 2, pp. 457–470, Mar. 1996.

[20] F. X. Kneizys et al., "The MODTRAN 2/3 report and LOWTRAN 7 MODEL," Phillips Lab., Geophys. Directorate, Hanscom Air Force Base, MA, USA, Tech. Rep. PL-TR-92-2060, 1996. [Online]. Available: https://vdoc.pub/download/the-modtran-2-3-report-and-lowtran-7-model-3i63asu18vt0

[21] E. Borbas et al., "Global profile training database for satellite regression retrievals with estimates of skin temperature and emissivity," in *Proc. 14th Int. Studying Leadership Conf.*, 2005, pp. 763–770.

[22] J. A. Nelder and R. Mead, "A simplex method for function minimization," *Comput. J.*, vol. 7, no. 4, pp. 308–313, 1965.

[23] W. Verhoef, L. Jia, Q. Xiao, and Z. Su, "Unified optical-thermal four-stream radiative transfer theory for homogeneous vegetation canopies," *IEEE Trans. Geosci. Remote Sens.*, vol. 45, no. 6, pp. 1808–1822, Jun. 2007.

[24] S. Zhou and J. Cheng, "An improved temperature and emissivity separation algorithm for the advanced Himawari imager," *IEEE Trans. Geosci. Remote Sens.*, vol. 58, no. 10, pp. 7105–7124, Oct. 2020.

[25] H. Hashim, Z. A. Latif, and N. A. Adnan, "Urban vegetation classification with NDVI threshold value method with very high resolution (VHR) Pleiades imagery," *Int. Arch. Photogramm., Remote Sens. Spatial Inf. Sci.*, vol. 42, pp. 237–240, Oct. 2019.

[26] J. A. Augustine, J. J. DeLuisi, and C. N. Long, "SURFRAD-A national surface radiation budget network for atmospheric research," *Bull. Amer. Meteorol. Soc.*, vol. 81, no. 10, pp. 2341–2358, 2000.

[27] J. Cheng and S. Liang, "Estimating global land surface broadband thermal-infrared emissivity using advanced very high resolution radiometer optical data," *Int. J. Digit. Earth*, vol. 6, no. sup1, pp. 34–49, Dec. 2013.

[28] J. Cheng and S. Liang, "Estimating the broadband longwave emissivity of global bare soil from the MODIS shortwave albedo product," *J. Geophys. Res., Atmos.*, vol. 119, no. 2, pp. 614–634, Jan. 2014.

[29] J. Cheng, S. Liang, W. Verhoef, L. Shi, and Q. Liu, "Estimating the hemispherical broadband longwave emissivity of global vegetated surfaces using a radiative transfer model," *IEEE Trans. Geosci. Remote Sens.*, vol. 54, no. 2, pp. 905–917, Feb. 2016.

[30] H. E. Beck, N. E. Zimmermann, T. R. McVicar, N. Vergopolan, A. Berg, and E. F. Wood, "Present and future Köppen–Geiger climate classification maps at 1-km resolution," *Sci. Data*, vol. 5, no. 1, Oct. 2018, Art. no. 180214.

[31] Z. Wan and Z. Li, "Radiance-based validation of the v5 MODIS land-surface temperature product," *Int. J. Remote Sens.*, vol. 29, nos. 17–18, pp. 5373–5395, Sep. 2008.

[32] G. C. Hulley et al., "Validation and quality assessment of the ECOSTRESS level-2 land surface temperature and emissivity product," *IEEE Trans. Geosci. Remote Sens.*, vol. 60, pp. 1–23, 2022. Art. no. 5000523.

[33] M. Dai et al., "Stripe noise removal for the thermal infrared spectrometer of the SDGSAT-1," *Int. J. Appl. Earth Observ. Geoinf.*, vol. 129, May 2024, Art. no. 103847.

[34] J. Ma et al., "An atmospheric influence correction method for longwave radiation-based in-situ land surface temperature," *Remote Sens. Environ.*, vol. 293, Aug. 2023, Art. no. 113611.